

Competing magnetic states in a non-coplanar Kagome magnet

Xiaodong Hu¹, Amar Fakhredine², Roger Guzman³, Martin Frentrup¹, Jinan Shi³, Giulio I. Lampronti¹, Sami El-Khatib⁴, Waichuen Tse⁵, Laura Gorzawski¹, Angelo Di Bernardo^{6,7}, Nadia Stelmashenko¹, Wu Zhou³, Mehmet Egilmez^{4,8}, Danfeng Li⁵, Grzegorz P. Mazur⁹, Mario Cuoco¹⁰, Carmine Autieri^{2,10}, Jason W. A. Robinson^{1✉}

¹Department of Materials Science & Metallurgy, University of Cambridge, 27 Charles Babbage Road, Cambridge, CB3 0FS, United Kingdom

²International Research Centre Magtop, Institute of Physics, Polish Academy of Sciences, Aleja Lotników 32/46, Warsaw, PL-02668, Poland

³School of Physical Sciences, University of Chinese Academy of Sciences, Huairou District, Beijing, 100049, China

⁴Department of Physics, American University of Sharjah, University City, Sharjah, 26666, United Arab Emirates

⁵Department of Physics, City University of Hong Kong, 83 Tat Chee Ave, Kowloon Tong, Hong Kong, China

⁶Department of Physics, University of Salerno, Via Giovanni Paolo II 132, Fisciano SA, 84084, Italy

⁷Department of Physics, University of Konstanz, Universitätsstraße 10, Konstanz, 78464, Germany

⁸Materials Research Center, American University of Sharjah, University City, Sharjah, 26666, United Arab Emirates

⁹Department of Materials, University of Oxford, Parks Road, Oxford, OX1 3PH, United Kingdom

¹⁰SPIN-CNR, UOS Salerno Fisciano (SA), IT-84084, Italy

[✉]Corresponding author: jjr33@cam.ac.uk

Abstract

Non-collinear Kagome antiferromagnets (AFMs) Mn_3X ($X = Sn, Ga, Ge, Ir, Pt$) can generate an anomalous Hall effect (AHE) despite vanishing net magnetization, enabled by broken time-reversal and inversion symmetries [1]. However, strong in-plane anisotropy has limited studies of the AFM-AHE and electronic applications to coplanar spin configurations. Non-coplanar spin textures in these systems have been realized only in low temperature spin-glass states [2, 3] or at interfaces with heavy metals [4, 5]. Here, we report an intrinsic non-coplanar spin configuration persisting up to 400 K in cubic-phase Mn_3Ge , originating from coexisting symmetric and antisymmetric exchange interactions. Competing magnetic states associated with this non-coplanar spin configuration give rise to an unconventional AHE with a magnetic-field-induced sign reversal and a hump-like feature. Our findings establish a platform for non-coplanar magnetism in AFM spintronics.

1 Introduction

Antiferromagnetic (AFM) materials are promising for spintronic applications because of the absence of a net magnetic moment in zero field, robustness against magnetic perturbations, and fast spin dynamics [6]. However, in contrast to ferromagnetic (FM) materials, AFMs typically exhibit weak electrical readout signals due to the cancellation of magnetotransport contributions. Therefore, identifying AFMs that can generate large magnetotransport effects is essential for the development of AFM spintronics. Among them, non-collinear Kagome AFMs Mn_3X ($X = Sn, Ga, Ge, Ir, Pt$) are of particular interest because their chiral spin textures break time-reversal symmetry and, when combined with spin-orbit coupling (SOC), generate a finite Berry curvature in momentum space and a large anomalous Hall effect (AHE) [7–17]. Electrical switching of non-collinear AFM order via spin-orbit torque has been demonstrated in Mn_3X , with tunneling magnetoresistance values of up to 100%, establishing a framework for AFM spintronics [18, 19].

While previous studies have focused on the coplanar non-collinear spin states of Kagome Mn_3X [20], non-coplanar spin textures and their associated magnetotransport properties are less well understood. One reason is the strong in-plane anisotropy in Mn_3X requires a large magnetic field to cant the spins out of the Kagome plane. Non-coplanar spin states have been observed only in the spin glass state (SGS) of

Mn_3Sn below 50 K [2, 3] or via interfacial spin-orbit coupling (SOC) at Pt/ Mn_3Sn interfaces [4, 5]. Here, we report on thin films of cubic-phase Mn_3Ge with an intrinsic non-coplanar spin texture originating from coexisting symmetric and antisymmetric exchange interactions. This spin configuration generates competing stable and metastable magnetic states within a single structural phase. Transitions between these magnetic states give rise to an unconventional AHE characterized by a magnetic-field-induced sign reversal and a hump-like feature, which are absent in coplanar Kagome AFMs.

2 Results

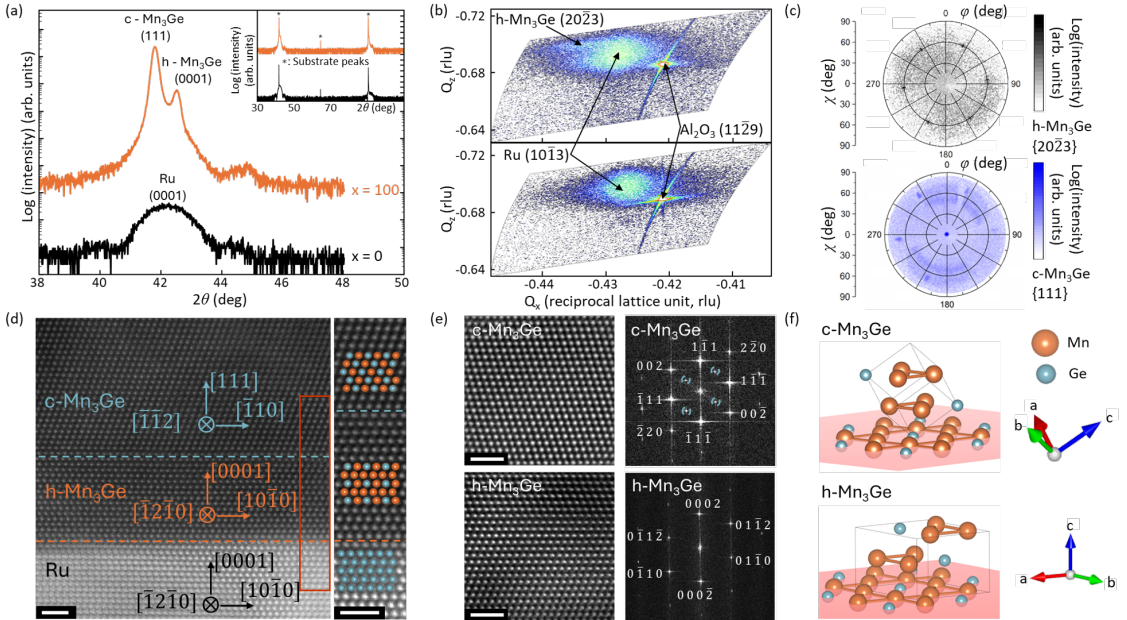


Fig. 1 (a) 2θ - ω XRD scans with a 0.2° ω offset of Mn_3Ge (x nm)/Ru (5 nm)/ Al_2O_3 films labeled with the structural phases. The inset shows scans without ω offset in a larger 2θ - ω range. (b) RSMs of a Mn_3Ge (100 nm)/Ru (5 nm)/ Al_2O_3 film (top) and a Ru (5 nm)/ Al_2O_3 film (bottom), labeled with reflections of h- Mn_3Ge (2023), Ru (1013), and Al_2O_3 (1129) planes. (c) χ - ϕ pole figures of a Mn_3Ge (100 nm)/Ru (5 nm)/ Al_2O_3 film aligning on h- Mn_3Ge (2023) (top) and c- Mn_3Ge (111) (bottom) reflections. (d) Cross-sectional STEM-HADDIF image of a Mn_3Ge (100 nm)/Ru (5 nm)/ Al_2O_3 film, viewed along the [1100] zone axis of the Al_2O_3 substrate. The boxed region is enlarged at right and matched with atomic models. The scale bars represent 1 nm. (e) STEM-HADDIF images (left) and corresponding FFT patterns (right) for h- Mn_3Ge and c- Mn_3Ge regions. Reflections in the FFT patterns are indexed, and the superlattice reflections of c- Mn_3Ge are indicated in the top-right panel. Scale bars represent 1 nm. (f) Atomic models of c- Mn_3Ge (top) and h- Mn_3Ge (bottom).

We deposited textured Mn_3Ge thin films by magnetron sputtering onto Ru-buffered Al_2O_3 (0001) substrates. In bulk material, h- Mn_3Ge is the thermodynamically stable phase with space group $\text{P}6_3/\text{mmc}$ (No. 194), while c- Mn_3Ge has a centrosymmetric structure with space group $\text{Pm}\bar{3}\text{m}$ (No. 221) [21]. Out-of-plane X-ray diffraction (XRD) 2θ - ω scans, collected in a coupled geometry with an incident angle offset of 0.2° in ω [Fig. 1(a)], show the (0001) h- Mn_3Ge and (111) c- Mn_3Ge reflections. Additional scans over a large range of $30^\circ \leq 2\theta \leq 110^\circ$ do not show any other detectable phases. Reciprocal space maps (RSM) comparing a 100-nm-thick Mn_3Ge film grown on Ru/ Al_2O_3 [Fig. 1(b), top] with a Ru/ Al_2O_3 reference sample [Fig. 1(b), bottom] show the (1013) Ru and (1129) Al_2O_3 reflections and that the Ru and Al_2O_3 are 30° rotated to another. This rotation corresponds to the honeycomb epitaxial growth of Ru on Al_2O_3 (0001) [22], providing a template on which h- Mn_3Ge grows by matching a doubled in-plane Ru unit cell without rotation. The in-plane epitaxial relationship between the hexagonal and cubic phases was confirmed by pole-figure measurements [Fig. 1(c)]. Both the {2023} h- Mn_3Ge and {111} c- Mn_3Ge reflections have matching patterns with sixfold symmetry due to similar atomic arrangements in their Kagome planes [Fig. 1(f)].

Cross-sectional scanning transmission electron microscopy high-angle annular dark-field (STEM-HADDIF) imaging [Fig. 1(d)] shows a sharp and continuous interface, and confirms the epitaxial relation-

ship $\text{Al}_2\text{O}_3(0001)[\bar{2}\bar{1}\bar{1}0] \parallel \text{Ru}(0001)[10\bar{1}0] \parallel \text{h-Mn}_3\text{Ge}(0001)[10\bar{1}0] \parallel \text{c-Mn}_3\text{Ge}(111)[\bar{1}\bar{1}0]$. The enlarged region (right panel), aligned with the atomic models, reveals a structural transition within the Mn_3Ge layer: the first 3–5 nm adjacent to the Ru buffer exhibits the hexagonal phase, above which the film converts to the cubic phase. Fast Fourier transform (FFT) patterns of c- Mn_3Ge and h- Mn_3Ge regions are consistent with the expected diffraction patterns of the two phases [Fig. 1(e)]. The superlattice reflections in c- Mn_3Ge regions arise from the ordered repetition of Mn and Ge atomic arrays, indicating high crystalline quality. Atomic models of the two phases, highlighting the resolved structural motifs, are shown in Fig. 1(f).

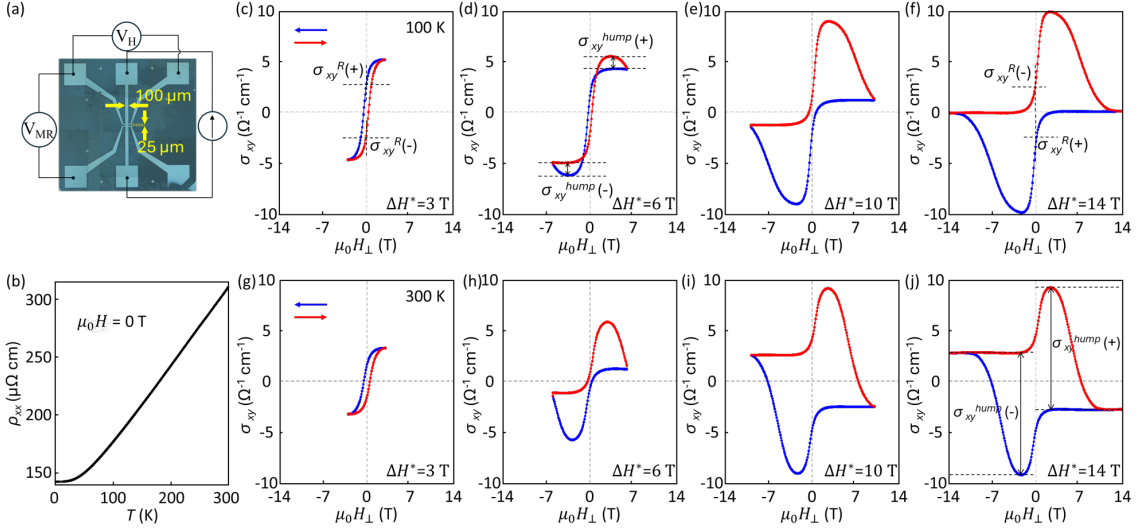


Fig. 2 (a) The Hall-bar geometry used in magnetotransport measurements of a 100-nm-thick Mn_3Ge film, labeled with Hall-bar dimensions. (b) Temperature dependence longitudinal resistivity. σ_{xy} hysteresis loops at 100 K (c)-(f) and 300 K (g)-(j), measured over $\Delta H^* = 3, 6, 10$, and 14 T. The blue (red) line corresponds to the field sweep from positive to negative (negative to positive).

We measured magnetotransport properties of a 100-nm-thick Mn_3Ge film in a Hall-bar geometry [Fig. 2(a)], varying the temperature and maximum field sweep range (ΔH^*). The magnetic field was applied perpendicular to the film plane (along the h- Mn_3Ge [0001] and c- Mn_3Ge [111] directions). The zero-field longitudinal resistivity (ρ_{xx}) varies smoothly with temperature from 2 K to 300 K without any low-temperature upturn or kink, indicating the absence of a SGS transition [Fig. 2(b)]. We calculated the Hall conductivity (σ_{xy}) from the measured Hall voltage by removing the ordinary Hall effect (OHE) and normalizing by the film thickness and longitudinal resistivity [23]. This normalization allows a direct comparison of σ_{xy} across films of different thicknesses and at different temperatures.

We extract the Hall conductivity remanence (σ_{xy}^R) from the hysteresis loops [Figs. 2(c-f,g-j)], defined as $\sigma_{xy}^R(+)-\sigma_{xy}^R(-)$ [Figs. 2(c,f)]. Here, $\sigma_{xy}^R(+)$ [$\sigma_{xy}^R(-)$] are the zero-field value of σ_{xy} after sweeping the magnetic field down from positive (up from negative) values. For small ΔH^* [Figs. 2(c,g)], the shape of the loops matches a conventional FM with positive σ_{xy}^R and positive σ_{xy} at maximum magnetic field. As ΔH^* increases [Figs. 2(d-f,h-j)], σ_{xy}^R and σ_{xy} at maximum field reverses in sign from positive to negative, and the loops develop flat regions and hump-like features. For example, in Fig. 2(j), as the field is swept from +14 T down to -14 T, σ_{xy} remains approximately constant until about 0 T in the flat region, then decreases to form a hump with a minimum near -3 T. On the return sweep (-14 T to +14 T), σ_{xy} stays flat until about 0 T and then increases to a maximum around +3 T.

The hump regions extend over a relatively wide range of magnetic fields, indicating that the feature is robust against the applied field. We quantify the hump amplitude by $\sigma_{xy}^{\text{hump}} = [|\sigma_{xy}^{\text{hump}}(+)| + |\sigma_{xy}^{\text{hump}}(-)|]/2$ [Figs. 2(d,j)]. Here, $\sigma_{xy}^{\text{hump}}(+)$ is the difference between the peak σ_{xy} and the flat-region σ_{xy} on the positive-field branch, and $\sigma_{xy}^{\text{hump}}(-)$ is the corresponding difference on the negative branch. At low ΔH^* , when the peak σ_{xy} equals that of the flat region, the hump amplitude vanishes [Figs. 2(c,g)].

Transport measurements on Mn_3Ge films with thicknesses less than 5 nm, where the structure is predominantly hexagonal, are shown in the Supplementary Information [23]. After subtracting the OHE, the Hall signal is negligible compared with that in the cubic phase, consistent with previous studies [11–13, 24]. Hence, the sign reversal and the hump feature are related to c- Mn_3Ge .

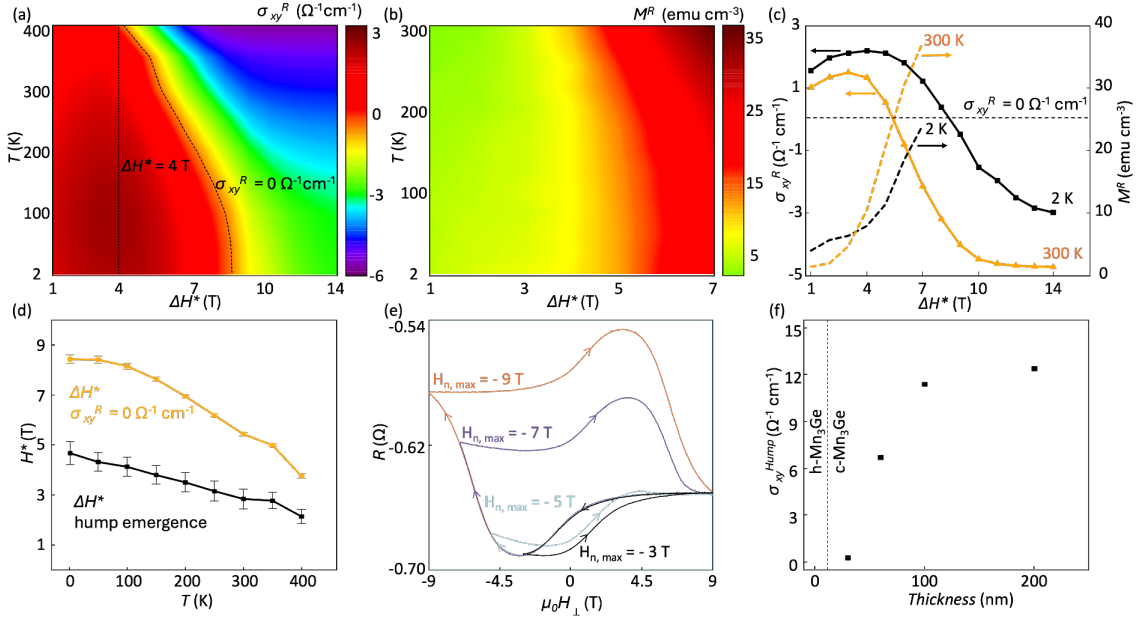


Fig. 3 (a) Color map of σ_{xy}^R as a function of ΔH^* (1–14 T) and temperature (2–400 K). Dashed lines indicate where $\Delta H^* = 4$ T and where $\sigma_{xy}^R = 0$. (b) Color map of M^R as a function of ΔH^* (1–7 T) and temperature (2–300 K). (c) M^R (dashed lines) σ_{xy}^R (solid lines) as functions of ΔH^* at 2 K and 300 K. The horizontal dashed line indicates where $\sigma_{xy}^R = 0$. (d) ΔH^* at which the hump emerges and at which the sign of σ_{xy}^R reverses as functions of temperature. (e) Minor hysteresis loops of σ_{xy} from a 100-nm-thick Mn₃Ge film at 300 K, labeled with the maximum negative field $H_{n,\max}$. (f) Hump magnitude $\sigma_{xy}^{\text{hump}}$ as a function of film thickness at 300 K measured over $\Delta H^* = 9$ T. The vertical dashed line indicates the hexagonal-cubic interface region.

We mapped the evolution of σ_{xy}^R and $\sigma_{xy}^{\text{hump}}$ for $\Delta H^* = 1–14 T over a temperature range of 2–400 K. As shown in Fig. 3(a), σ_{xy}^R increases with ΔH^* at small ΔH^* , then decreases and reverses in sign at large ΔH^* . In contrast, the magnetization remanence M^R [Fig. 3(b)], defined similarly to σ_{xy}^R , grows monotonically with ΔH^* . The extracted 2 K and 300 K trends [Fig. 3(c)] highlight this contrast: σ_{xy}^R increases with ΔH^* up to around 4 T, then decreases and reverses in sign between ΔH^* of 5 T to 9 T depending on temperature, whereas M^R remains positive and grows monotonically with ΔH^* . Thus, the sign reversal and hump feature cannot be accounted for by a magnetization-driven AHE alone.$

In hysteresis loops measured over a field range of $\Delta H^* = 10$ T [Figs. 2(e,i)], $\sigma_{xy}^{\text{hump}}$ at 300 K is larger than that at 2 K, and σ_{xy}^R reverses in sign between the two temperatures. This indicates that the ΔH^* values required for the hump emergence and the sign reversal depend on temperature. As shown in Fig. 3(d), the hump emerges at ΔH^* around 5 T and σ_{xy}^R reverses sign near 9 T at 2 K, whereas at 300 K these features occur at approximately 3 T and 5.5 T, respectively. Therefore, the magnetic field required to trigger these anomalous behaviors decreases as the temperature increases. The critical ΔH^* for the sign reversal in σ_{xy}^R is always larger than that for the hump emergence.

3 Discussion

The results highlight two key features in the behavior of σ_{xy} depending on the field sweep range and temperature: (1) an enhancement of σ_{xy} , which coincides with a hump-like feature; (2) a sign reversal of σ_{xy}^R and σ_{xy} at the highest applied field. In general, hump-like features in Hall measurements can be attributed to a topological Hall effect (THE) from real-space Berry curvature [2–5, 25], or to the superposition of opposing AHE channels from momentum-space Berry curvature [26–28] (with or without a sign reversal of σ_{xy}). In principle, both mechanisms are plausible for c-Mn₃Ge. Out-of-plane spin canting in a Kagome spin arrangement could produce a finite solid angle, leading to nonzero scalar spin chirality and real-space Berry curvature. Alternatively, the coexistence of h-Mn₃Ge, c-Mn₃Ge, and their interface could give rise to multiple AHE contributions with opposite signs.

To investigate whether the hump originates from a THE, we measured minor loops of σ_{xy} , in which the magnetic field is swept from 9 T to a negative value and then back to 9 T. The maximum negative

field reached in a minor loop is referred to as $H_{n,\max}$ [Fig. 3(e)]. We find that the hump feature is hysteretic: its emergence on the positive-field branch depends on whether $H_{n,\max}$ exceeds the field at which the hump appears on the negative-field branch. At 300 K, the hump on the negative branch emerges once the field exceeds about -3.5 T, and it vanishes on the positive branch if $H_{n,\max}$ is limited to -3 T. This is inconsistent with a scalar-chirality-driven THE arising from out-of-plane canting [29]: if the hump were caused by such canting, the canting at a given positive magnetic field would depend only on that magnetic field, not on the applied magnetic field history.

Although the AHE from the (0001)-oriented hexagonal phase is negligible, as shown in previous studies and Supplementary Information [11, 12, 23, 24], the superposition of two AHE channels with opposite signs – one from the cubic phase and the other from the hexagonal-cubic interface – could in principle produce a hump [30]. Therefore, we investigated the thickness dependence of $\sigma_{xy}^{\text{hump}}$ from Mn₃Ge films of 30, 60, 100, and 200 nm [Fig. 3(f)]. The $\sigma_{xy}^{\text{hump}}$ increases monotonically from 30 to 100 nm and then saturates at larger thicknesses. As shown in Fig. 1(d), c-Mn₃Ge grows on h-Mn₃Ge at a film thickness of 3–5 nm, and the hexagonal-cubic interface appears around this thickness. Therefore, the AHE contribution from the interface should remain constant for all films thicker than 5 nm, whereas the AHE from c-Mn₃Ge should continue to increase with thickness. If the hump is caused by the superposition of the two AHE channels from c-Mn₃Ge and from the interface with opposite signs, $\sigma_{xy}^{\text{hump}}$ would eventually decrease with increasing thickness as the AHE from c-Mn₃Ge dominates. Therefore, the monotonic increase of $\sigma_{xy}^{\text{hump}}$ with film thickness is incompatible with this two-channel AHE scenario.

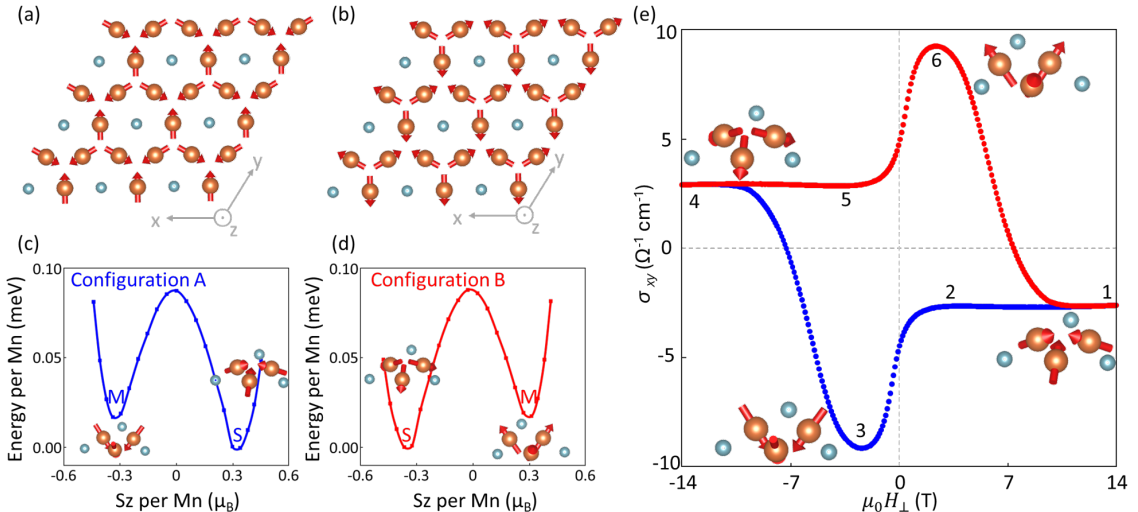


Fig. 4 Spin configurations A (a) and B (b) in c-Mn₃Ge [21]. The large and small spheres represent Mn and Ge atoms, respectively, and the red arrows represent the spin directions. The x , y , and z axes correspond to the [112], [121], and [111] axes in c-Mn₃Ge, respectively. Total energy as a function of the out-of-plane canting for spin configurations A (c) and B (d), labeled with the stable (S) and the metastable (M) states. (e) A σ_{xy} hysteresis loop from a 100-nm-thick film at 300 K over a magnetic field sweep range of $\Delta H^* = 14$ T, labeled with magnetic states 1–6. The schematics in (c), (d), and (e) illustrate the out-of-plane spin canting.

To investigate the origin of the hump-like feature and the sign reversal, we performed density functional theory (DFT) calculations for c-Mn₃Ge. In non-collinear Kagome AFMs, vector chirality characterizes the magnetic ground state by describing the spin rotation in a triangular arrangement of three Mn atoms. When moving anticlockwise from one Mn atom to the next, the spins rotate anticlockwise for a chirality of +1 and clockwise for a chirality of -1. The ground-state chirality of c-Mn₃Ge is +1 [21], consisting of two degenerate spin configurations A and B, as shown in Figs. 4(a,b). The two configurations may coexist in different magnetic domains and generate opposite signs of σ_{xy} through the momentum-space Berry curvature [31, 32]. This Berry curvature is influenced by the Weyl points (connected by inversion symmetry) and semi-Dirac points near the Fermi level in the band structure [21, 23].

We define the z axis along the [111] direction of c-Mn₃Ge (along which the magnetic field is applied in magnetotransport measurements). Within relativistic DFT calculations, c-Mn₃Ge can exhibit a magnetic solution with vanishing magnetization along z , consistent with previous studies [12, 21, 33]. However, by uniformly increasing the initial values of the spin component along z (S_z) on all Mn

atoms, the system converges to FM solutions with finite magnetization. This indicates the presence of a symmetric exchange interaction in c-Mn₃Ge that induces FM coupling for S_z . In Kagome AFMs, the dominant exchange interaction between Mn atoms is antiferromagnetic among the in-plane spin components, stabilizing an all-in- or all-out-type ground state [34]. The persistence of the AHE up to 400 K indicates that the in-plane AFM interactions remain robust despite the geometric frustration of the Kagome lattice. To account for the two distinct exchange interactions, we describe the system using an XXZ Hamiltonian [35]:

$$H = \sum_{i < j} [J_{ij}^{\parallel} (S_i^x S_j^x + S_i^y S_j^y) + J_{ij}^{\perp} S_i^z S_j^z], \quad (1)$$

where S_i^{α} denotes the spin component at site i along direction α , $J^{\parallel} > 0$ is the strong AFM in-plane exchange coupling, and $J^{\perp} < 0$ is the FM out-of-plane exchange coupling. It was shown that the first neighbor interaction dominates in intermetallic compounds with Kagome lattices [36]. The opposite signs of the first-neighbor J^{\parallel} and J^{\perp} suggest an indirect Ruderman–Kittel–Kasuya–Yosida (RKKY) exchange mechanism mediated by conduction electrons. The RKKY exchange is known to oscillate in sign depending on the Fermi surface, which allows different signs for J^{\parallel} and J^{\perp} [37]. Consequently, the coexistence of the in-plane AFM coupling ($J^{\parallel} > 0$) and the out-of-plane FM coupling ($J^{\perp} < 0$) in c-Mn₃Ge arises within an XXZ description governed by RKKY exchange interaction.

The symmetric FM exchange interaction produces an even double-well energy profile as a function of S_z , which is identical for spin configurations A and B and exhibits two degenerate minima at opposite canting directions. In contrast, due to SOC and broken PT symmetry, the antisymmetric Dzyaloshinskii–Moriya interaction (DMI) induces a weak ferromagnetism via spin canting out of the Kagome plane and favors one canting direction over the other. This preferred canting direction is reversed between spin configurations A and B. Therefore, the DMI contributes an energy term that is odd in S_z [38], and the sign of this energy contribution is opposite for the two spin configurations. As detailed in the Supplementary Information [23], the coexistence of symmetric and antisymmetric exchange interactions gives rise to the energy profiles shown in Figs. 4(c,d) as functions of S_z . For each spin configuration, two local energy minima are related by a mirror reflection of spin canting with respect to the Kagome plane. Since mirror symmetry is absent in the system, reflecting the spins across the Kagome plane produces a stable ground state (S) and a higher-energy metastable state (M). These minima are shifted in opposite canting directions for the two configurations: configuration A has a stable state with $S_z > 0$ and a metastable state with $S_z < 0$, whereas configuration B shows the opposite. Both exchange interactions act along the z direction, while the net magnetization within the Kagome plane remains zero.

We propose that the field-driven transitions between these four states in two spin configurations cause the hump-like features and the sign reversal in the AHE. We consider the AHE over $\Delta H^* = 14$ T by the numbered states in Fig. 4(e). At positive saturation (state 1), the system is in a stable ground state with spins canting up (stable A state), corresponding to a negative σ_{xy} . This state persists as the magnetic field is swept towards 0 T (states 1 to 2), producing the flat region. As the magnetic field is swept from positive to negative values, two competing processes occur simultaneously:

- (1) the stable A state converts to the metastable A state with spins canting down;
- (2) the metastable A state converts to the stable B state with in-plane spin reorientation.

Since process (2) requires additional energy for the in-plane spin reorientation vs process (1), process (1) and metastable A state dominate at low field (states 2 to 3). The larger $|\sigma_{xy}|$ at state 3 than that at state 1 indicates an enhanced σ_{xy} in the metastable state vs the stable state, consistent with theoretical predictions [39, 40]. Upon further increase of the magnetic field (states 3 to 4), process (2) and stable B state dominate, with σ_{xy} of opposite sign to configuration A, and the net value of σ_{xy} approaches 0 before reversing in sign. The transitions between the magnetic states during the magnetic field sweep back are similar. Stable B state persists until about 0 T (states 4 to 5) in the flat region, and then two competing processes occur as the field is swept from negative to positive values: (1) the stable B state converts to the metastable B state, and (2) the metastable B state converts to the stable A state. The metastable B state dominates at low field (states 5 to 6) with a larger $|\sigma_{xy}|$ than the stable B state, causing the increase in σ_{xy} . The stable A state dominates at high field (states 6 to 1) with σ_{xy} opposite in sign to configuration B, and the net value of σ_{xy} approaches 0 before reversing in sign.

In general, the emergence of the hump and the sign of σ_{xy} at maximum field depends on a competition between two processes as the field is swept:

- (1) the conversion of the stable state into the metastable state with the same in-plane spin configuration, which increases $|\sigma_{xy}|$;

- (2) the conversion of the metastable state into the stable state with a different in-plane spin configuration, which decreases the $|\sigma_{xy}|$ and then reverses its sign.

Process (1) and the metastable states dominate at low magnetic field, while process (2) and the stable states dominate at high field. The relative influence of processes (1) and (2) determines the shape of the hysteresis loop. For small ΔH^* [Fig. 2(c,g)], process (1) and the metastable states dominate during the entire loop. Therefore, σ_{xy} varies without a hump and the σ_{xy} at the maximum field is determined by the metastable states (positive at positive field). For intermediate ΔH^* [Fig. 2(d,h)], there is a critical field where the rate of increase in $|\sigma_{xy}|$ from process (1) equals to the rate of decrease in $|\sigma_{xy}|$ from process (2). At this point, the net value of $|\sigma_{xy}|$ reaches a maximum and forms a hump before decreasing. Therefore, the hump appears once ΔH^* is high enough that both processes occur at the same rate. Upon further increase in ΔH^* [Figs. 2(f,j)], σ_{xy} from the stable state cancels out that from the metastable state, and σ_{xy} at the maximum field in the loop goes to 0 and reverses in sign.

We note that the hump region in the hysteresis loop corresponds to a mixed domain structure: some domains are converting from the stable state to the metastable state with the same in-plane spin configuration, and some are converting from the metastable state to the stable state with a different in-plane configuration. This coexistence of domains broadens the hump feature, causing it to span a wider field range than reported in other materials [2–5, 25–27]. The temperature dependence of the hump emergence and the sign reversal of σ_{xy} shows that the ΔH^* required for these features decreases with increasing temperature [Fig. 3(d)]. This suggests that thermal fluctuations provide energy to facilitate both the out-of-plane spin canting reversal in process (1) and the in-plane spin reorientation in process (2). Thermal fluctuations have been reported to promote out-of-plane canting in the paramagnetic regime of Kagome systems [41]. Whether a similar thermal effect could also operate in the AFM state requires further study.

In summary, the magnetic field drives the system through different magnetic states, and the field-sweep range ΔH^* determines which states are accessed within a hysteresis loop. At small ΔH^* , even at the highest field, the system remains in a metastable-state-dominated regime, generating a hysteresis loop with no hump and positive σ_{xy}^R . At intermediate ΔH^* , the loop enters a mixed regime before reaching the maximum field: the σ_{xy} from the stable state starts to dominate but has not yet fully cancel that from the metastable state, producing a hump in the loop and σ_{xy}^R remains positive. For large ΔH^* , the system goes through a metastable-dominated regime, then a mixed regime, and finally into a stable-state-dominated regime, generating a hump and a negative σ_{xy}^R . Therefore, different field sweep ranges produce distinct loop shapes, reflecting the different sequences of magnetic state transitions during the field sweep.

Unlike the cubic phase, h-Mn₃Ge lacks the combination of FM interaction, DMI, and associated S_z canting that gives rise to two energy minima. Consequently, the hexagonal structure has neither a metastable magnetic state nor an A–B spin configuration switching under a magnetic field. Therefore, no hump or σ_{xy}^R sign reversal has been observed in h-Mn₃Ge either in our measurements or in previous studies [11–13, 23, 24].

4 Conclusion

We have demonstrated that cubic-phase Kagome Mn₃Ge exhibits an AHE with a sign reversal and a hump-like feature in σ_{xy} up to 400 K. These phenomena originate from a non-coplanar spin configuration emerging from the non-collinear AFM state. Our theoretical analysis shows that this spin texture results from the coexistence of conventional ferromagnetism induced by a symmetric RKKY exchange and weak ferromagnetism induced by an antisymmetric DMI. This coexistence produces an unconventional energy profile with a stable and a metastable magnetic state. Transitions between these states give rise to the sign reversal and the hump-like features in the AHE. From a thermodynamic perspective, a system hosting coexisting ferromagnetic and weak-ferromagnetic order along the same direction can exhibit behavior deviating from those of the conventional ferromagnetic or weak-ferromagnetic universality classes.

Hump-like features in the Hall effect, with or without a sign reversal, have previously been attributed either to real-space Berry-curvature effects – such as skyrmions [42–44] and other engineered systems [2–5], often enabled by heavy-element-induced SOC – or to multiple AHE channels arising from structural phase coexistence [26–28]. Here, we demonstrate an alternative route to achieve these features in a single phase driven by the competition between magnetic states and the resulting changes in the momentum-space Berry curvature that underlie the AHE.

These results highlight the sensitivity of the electronic band structure to the spin texture and provide a platform to engineer momentum-space Berry curvature using an applied magnetic field in AFMs. In this way, cubic Mn_3Ge offers a versatile system for exploring non-coplanar AFM spintronics. Further studies of the spin dynamics associated with these state transitions will be important for a complete understanding of the underlying mechanisms.

5 Acknowledgement

R.G. was supported by the CAS Project for Young Scientists in Basic Research (YSBR-003), the National Natural Science Foundation of China (grant No. 52373231), and the Beijing Outstanding Young Scientist Program (No. BJJWZYJH01201914430039). This research benefited from resources and support from the Electron Microscopy Center at the University of Chinese Academy of Sciences. C.A. was supported by the "MagTop" project (FENG.02.01-IP.05-0028/23) carried out within the "International Research Agendas" programme of the Foundation for Polish Science, co-financed by the European Union under the European Funds for Smart Economy 2021-2027 (FENG). C.A. and M.C. acknowledge support from PNRR MUR project PE0000023-NQSTI. We further acknowledge access to the computing facilities of the Interdisciplinary Center of Modeling at the University of Warsaw, Grant g91-1418, g91-1419, g96-1808 and g96-1809 for the availability of high-performance computing resources and support. We acknowledge the access to the computing facilities of the Poznan Supercomputing and Networking Center, Grants No. pl0267-01, pl0365-01 and pl0471-01.

6 Methods

6.1 Sample preparation

The thin films were deposited by magnetron sputtering in an ultra-high-vacuum system with a base pressure below 1×10^{-8} Torr. $\text{Al}_2\text{O}_3(0001)$ substrates were loaded through a load-lock system without any additional surface preparation and were rotated at 10 rpm during deposition to ensure uniform film growth. The growth temperature was controlled by a radiative heater mounted on the back of the sample holder. The Ru buffer layer was deposited at 700 °C by a radio-frequency (r.f.) power of 30 W in an Ar pressure of 1.5 mTorr. The Mn_3Ge layer was subsequently deposited from a Mn_3Ge alloy target at 700 °C by a direct-current (d.c.) power of 30 W in an Ar pressure of 2 mTorr. The Hall bar geometries [Fig. 2(a)] were fabricated by optical lithography and Ar ion-beam etching.

6.2 Structural characterization

X-ray diffraction characterizations were performed using a four-circle Panalytical Empyrean vertical ω/θ diffractometer equipped with a hybrid two-bounce primary monochromator. A proportional counter was used for the $2\theta-\omega$ and ϕ scans, and a two-dimensional PIXCEL position-sensitive detector (PSD) was used to collect reciprocal space maps (RSMs).

Cross-sectional samples for transmission electron microscopy were prepared by standard lift-out process using a focused ion beam (FIB) system Thermo Fischer Scientific Helios G4 CX Dual-Beam. To minimize the sidewall damage and sufficiently thin the specimen for electron transparency, final milling was carried out at low voltage (2 kV).

Atomic-resolution STEM-HAADF images were carried out in a JEOL GrandARM-2 operated at 200 kV. The annular detector collection semi-angles were set to 68–280 mrad for HAADF. EELS experiments were carried out in a NION U-HERMES microscope operated at 60 kV, equipped with a fifth-order aberration corrector, an alpha-type monochromator and the Dectris ELA direct electron detector for EELS acquisition. The experiments were conducted with beam convergence semi-angle and EELS collection semi-angle of 32 and 75 mrad, respectively, and an energy dispersion of 0.9 eV/ch and a pixel dwell time of 100 ms.

6.3 Transport and magnetization measurements

Longitudinal and transverse resistances were measured using the fabricated Hall bar geometries by a four-probe configuration in a Quantum Design Physical Property Measurement System (PPMS), with a Keithley 6221 current source and a Keithley 2182A nanovoltmeter. Magnetic measurements

were performed using a Quantum Design Magnetic Property Measurement System (MPMS3) with a vibrating sample magnetometer (VSM) and a superconducting quantum interference device (SQUID).

6.4 Density functional theory calculation

Density functional theory (DFT) calculations were performed using the Vienna *ab initio* Simulation Package (VASP) [45, 46] with the projector-augmented wave (PAW) method [47]. The exchange–correlation functional was described using the generalized gradient approximation (GGA) in the Perdew–Burke–Ernzerhof (PBE) form [48]. Periodic boundary conditions were applied, and the Bloch theorem was used to treat the crystalline system. The plane-wave cutoff energy was set to 390 eV, and the total energy convergence criterion was 10^{-4} eV. The Brillouin zone was sampled using a Monkhorst–Pack $16 \times 16 \times 12$ *k*-point mesh. To estimate the weak ferromagnetism, we used a reconstructed supercell oriented along the [111] direction of the cubic cell containing three formula units. The PAW potentials included 7 valence electrons for Mn and 4 for Ge, resulting in a total of 75 valence electrons for the 9 Mn and 3 Ge atoms in the supercell. The lattice parameters were taken from experiment as $a = b = 5.164$ Å and $c = 6.324$ Å. Maximally localized Wannier functions were constructed using the Mn 3d and Ge 4p orbitals as initial projections. These projections were used to obtain an accurate tight-binding Hamiltonian describing the low-energy electronic structure of the system.

References

- [1] Rimmller, B.H., Pal, B., Parkin, S.S.P.: Non-collinear antiferromagnetic spintronics. *Nature Reviews Materials* **10**(2), 109–127 (2025) <https://doi.org/10.1038/s41578-024-00706-w>
- [2] Rout, P.K., Madduri, P.V.P., Manna, S.K., Nayak, A.K.: Field-induced topological Hall effect in the noncoplanar triangular antiferromagnetic geometry of Mn₃Sn. *Physical Review B* **99**(9), 094430 (2019) <https://doi.org/10.1103/PhysRevB.99.094430>
- [3] Taylor, J.M., Markou, A., Lesne, E., Sivakumar, P.K., Luo, C., Radu, F., Werner, P., Felser, C., Parkin, S.S.: Anomalous and topological Hall effects in epitaxial thin films of the noncollinear antiferromagnet Mn₃Sn. *Physical Review B* **101**(9), 094404 (2020) <https://doi.org/10.1103/physrevb.101.094404>
- [4] Liu, X., Feng, Q., Zhang, D., Deng, Y., Dong, S., Zhang, E., Li, W., Lu, Q., Chang, K., Wang, K.: Topological Spin Textures in a Non-Collinear Antiferromagnet System. *Advanced Materials*, 2211634 (2023) <https://doi.org/10.1002/adma.202211634>
- [5] Cheng, Y., Yu, S., Zhu, M., Hwang, J., Yang, F.: Tunable topological Hall effects in noncollinear antiferromagnet Mn₃Sn/Pt bilayers. *APL Materials* **9**(5) (2021) <https://doi.org/10.1063/5.0048733>
- [6] Jungwirth, T., Marti, X., Wadley, P., Wunderlich, J.: Antiferromagnetic spintronics. *Nature Nanotechnology* **11**(3), 231–241 (2016) <https://doi.org/10.1038/nnano.2016.18>
- [7] Kagome Mn₃X have two structural phases: a hexagonal phase (X = Sn, Ga, Ge) and a cubic phase (X = Ir, Pt). In the hexagonal phases, a small net in-plane magnetic moment allows an applied magnetic field to reorient the AFM domains and to control the AHE [12]. In principle, strong magnetocrystalline anisotropy in the cubic phases suppresses any net in-plane moment, leading to a cancellation of AHE contributions from domains with opposite chirality [31]. However, the observation of a finite AHE arising from epitaxial strain or spin canting in cubic systems [16, 17], together with theoretical predictions of parity–time (PT) symmetry breaking, weak ferromagnetism, and spin–momentum locking [49, 50], reveals the rich physics of the cubic phase.
- [8] Nakatsuji, S., Kiyohara, N., Higo, T.: Large anomalous Hall effect in a non-collinear antiferromagnet at room temperature. *Nature* **527**(7577), 212–215 (2015) <https://doi.org/10.1038/nature15723>
- [9] Gas, K., Yoon, J.-Y., Sato, Y., Kubota, H., Dluzewski, P., Kret, S., Domagala, J., Edathumkandy, Y., Takeuchi, Y., Kanai, S., et al.: Magnetic phase diagram of Mn_{3+x}Sn_{1-x} epitaxial thin films: Extending the anomalous Hall effect to low temperatures via intrinsic alloying. *APL Materials* **13**(4) (2025) <https://doi.org/10.1063/5.0254918>

- [10] Song, L., Zhou, F., Li, H., Ding, B., Li, X., Xi, X., Yao, Y., Lau, Y.-C., Wang, W.: Large anomalous Hall effect at room temperature in a fermi-level-tuned kagome antiferromagnet. *Advanced Functional Materials* **34**(28), 2316588 (2024) <https://doi.org/10.1002/adfm.202316588>
- [11] Kiyohara, N., Tomita, T., Nakatsuji, S.: Giant Anomalous Hall Effect in the Chiral Antiferromagnet Mn₃Ge. *Physical Review Applied* **5**(6), 064009 (2016) <https://doi.org/10.1103/PhysRevApplied.5.064009>
- [12] Nayak, A.K., Fischer, J.E., Sun, Y., Yan, B., Karel, J., Komarek, A.C., Shekhar, C., Kumar, N., Schnelle, W., Kübler, J., Felser, C., Parkin, S.S.P.: Large anomalous Hall effect driven by a nonvanishing Berry curvature in the noncollinear antiferromagnet Mn₃Ge. *Science Advances* **2**(4), 1501870 (2016) <https://doi.org/10.1126/sciadv.1501870>
- [13] Chen, T., Tomita, T., Minami, S., Fu, M., Koretsune, T., Kitatani, M., Muhammad, I., Nishio-Hamane, D., Ishii, R., Ishii, F., Arita, R., Nakatsuji, S.: Anomalous transport due to Weyl fermions in the chiral antiferromagnets Mn₃Ge, X = Sn, Ge. *Nature Communications* **12**(1), 572 (2021) <https://doi.org/10.1038/s41467-020-20838-1>
- [14] Wen, C., Xiong, D., Yang, C., Zhu, D., Zhao, W.: Enhanced anomalous Hall conductivity via Ga doping in Mn₃Sn and Mn₃Ge. *Physical Review B* **112**(11), 115118 (2025) <https://doi.org/10.1103/tktp-dhvc>
- [15] Chen, H., Niu, Q., MacDonald, A.H.: Anomalous Hall Effect Arising from Noncollinear Antiferromagnetism. *Physical Review Letters* **112**(1), 017205 (2014) <https://doi.org/10.1103/PhysRevLett.112.017205>
- [16] Zuniga-Cespedes, B.E., Manna, K., Noad, H.M.L., Yang, P.-Y., Nicklas, M., Felser, C., Mackenzie, A.P., Hicks, C.W.: Observation of an anomalous Hall effect in single-crystal Mn₃Pt. *New Journal of Physics* **25**(2), 023029 (2023) <https://doi.org/10.1088/1367-2630/acbc3f>
- [17] Xu, S., Dai, B., Jiang, Y., Xiong, D., Cheng, H., Tai, L., Tang, M., Sun, Y., He, Y., Yang, B., Peng, Y., Wang, K.L., Zhao, W.: Universal scaling law for chiral antiferromagnetism. *Nature Communications* **15**(1), 3717 (2024) <https://doi.org/10.1038/s41467-024-46325-5>
- [18] Tsai, H., Higo, T., Kondou, K., Nomoto, T., Sakai, A., Kobayashi, A., Nakano, T., Yakushiji, K., Arita, R., Miwa, S., *et al.*: Electrical manipulation of a topological antiferromagnetic state. *Nature* **580**(7805), 608–613 (2020) <https://doi.org/10.1038/s41586-020-2211-2>
- [19] Qin, P., Yan, H., Wang, X., Chen, H., Meng, Z., Dong, J., Zhu, M., Cai, J., Feng, Z., Zhou, X.: Room-temperature magnetoresistance in an all-antiferromagnetic tunnel junction. *Nature* **613**(7944), 485–489 (2023) <https://doi.org/10.1038/s41586-022-05461-y>
- [20] Šmejkal, L., MacDonald, A.H., Sinova, J., Nakatsuji, S., Jungwirth, T.: Anomalous Hall antiferromagnets. *Nature Reviews Materials* **7**(6), 482–496 (2022) <https://doi.org/10.1038/s41578-022-00430-3>
- [21] Markou, A., Taylor, J.M., Gayles, J., Sun, Y., Kriegner, D., Grenzer, J., Guo, S., Schnelle, W., Lesne, E., Felser, C., Parkin, S.S.P.: Cubic Mn₃Ge thin films stabilized through epitaxial growth as a candidate noncollinear antiferromagnet. *Applied Physics Letters* **125**(2) (2024) <https://doi.org/10.1063/5.0206194>
- [22] Kurdi, S., Zilske, P., Xu, X.D., Frentrup, M., Vickers, M.E., Sakuraba, Y., Reiss, G., Barber, Z.H., Koo, J.W.: Optimization of ruthenium as a buffer layer for non-collinear antiferromagnetic Mn₃X films. *Journal of Applied Physics* **127**(16), 165302 (2020) <https://doi.org/10.1063/1.5140464>
- [23] Supplementary Information
- [24] Zhang, Y., Sun, Y., Yang, H., Železný, J., Parkin, S.P.P., Felser, C., Yan, B.: Strong anisotropic anomalous Hall effect and spin Hall effect in the chiral antiferromagnetic compounds Mn₃X (X=Ge, Sn, Ga, Ir, Rh, and Pt). *Physical Review B* **95**(7), 075128 (2017) <https://doi.org/10.1103/PhysRevB.95.075128> . PRB

- [25] Sürgers, C., Fischer, G., Winkel, P., Löhneysen, H.v.: Large topological Hall effect in the non-collinear phase of an antiferromagnet. *Nature Communications* **5**(1), 3400 (2014) <https://doi.org/10.1038/ncomms4400>
- [26] Ziese, M., Jin, L., Lindfors-Vrejoiu, I.: Unconventional anomalous Hall effect driven by oxygen-octahedra-tailoring of the SrRuO_3 structure. *Journal of Physics: Materials* **2**(3), 034008 (2019)
- [27] Kimbell, G., Sass, P.M., Woltjes, B., Ko, E.K., Noh, T.W., Wu, W., Robinson, J.W.A.: Two-channel anomalous Hall effect in SrRuO_3 . *Physical Review Materials* **4**(5), 054414 (2020) <https://doi.org/10.1103/PhysRevMaterials.4.054414>
- [28] Zhou, G., Kang, P., Ji, H., Dou, J., Wang, S., Xu, X.: Observation of two-channel anomalous Hall effect in perpendicularly magnetized NiCo_2O_4 epitaxial films. *Phys. Rev. B* **108**, 094442 (2023) <https://doi.org/10.1103/PhysRevB.108.094442>
- [29] Kan, D., Moriyama, T., Kobayashi, K., Shimakawa, Y.: Alternative to the topological interpretation of the transverse resistivity anomalies in SrRuO_3 . *Physical Review B* **98**(18), 180408 (2018) <https://doi.org/10.1103/PhysRevB.98.180408>
- [30] Kimbell, G., Kim, C., Wu, W., Cuoco, M., Robinson, J.W.: Challenges in identifying chiral spin textures via the topological Hall effect. *Communications Materials* **3**(1), 19 (2022) <https://doi.org/10.1038/s43246-022-00238-2>
- [31] Taylor, J.M., Lesne, E., Markou, A., Dejene, F.K., Sivakumar, P.K., Pöllath, S., Rana, K.G., Kumar, N., Luo, C., Ryll, H., et al.: Magnetic and electrical transport signatures of uncompensated moments in epitaxial thin films of the noncollinear antiferromagnet Mn_3Ir . *Applied Physics Letters* **115**(6) (2019) <https://doi.org/10.1063/1.5099428>
- [32] Zhang, W., Han, W., Yang, S.-H., Sun, Y., Zhang, Y., Yan, B., Parkin, S.S.: Giant facet-dependent spin-orbit torque and spin Hall conductivity in the triangular antiferromagnet IrMn_3 . *Science Advances* **2**(9), 1600759 (2016) <https://doi.org/10.1126/sciadv.1600759>
- [33] Soh, J.-R., De Juan, F., Qureshi, N., Jacobsen, H., Wang, H.-Y., Guo, Y.-F., Boothroyd, A.: Ground-state magnetic structure of Mn_3Ge . *Physical Review B* **101**(14), 140411 (2020) <https://doi.org/10.1103/physrevb.101.140411>
- [34] Sante, D.D., Neupert, T., Sangiovanni, G., Thomale, R., Comin, R., Checkelsky, J.G., Zeljkovic, I., Wilson, S.D.: Kagome metals. *Rev. Mod. Phys.*, (2025) <https://doi.org/10.1103/1g9n-wm38>
- [35] Chernyshev, A., Zhitomirsky, M.E.: Quantum selection of order in an XXZ antiferromagnet on a kagome lattice. *Physical Review Letters* **113**(23), 237202 (2014) <https://doi.org/10.1103/physrevlett.113.237202>
- [36] Sharma, S., Chioncel, L., Di Marco, I.: Exploring strong electronic correlations in the breathing kagome metal Fe_3Sn . *Phys. Rev. B* **111**, 235127 (2025) <https://doi.org/10.1103/xmmr-mfv4>
- [37] Itokazu, S., Kirikoshi, A., Jeschke, H.O., Otsuki, J.: From localized 4f electrons to anisotropic exchange interactions in ferromagnetic CeRh_6Ge_4 . *Communications Materials* **6**(1), 269 (2025) <https://doi.org/10.1038/s43246-025-00998-7>
- [38] Roig, M., Yu, Y., Ekman, R.C., Kreisel, A., Andersen, B.M., Agterberg, D.F.: Quasisymmetry-Constrained Spin Ferromagnetism in Altermagnets. *Physical Review Letters* **135**(1), 016703 (2025) <https://doi.org/10.1103/839n-rckn>
- [39] Brzezicki, W., Autieri, C., Cuoco, M.: Sign competing sources of Berry curvature and anomalous Hall conductance humps in topological ferromagnets. *Advanced Electronic Materials* **11**(18), 00307 (2025) <https://doi.org/10.1002/aelm.202500307>
- [40] Alam, M.S., Fakhredine, A., Ahmad, M., Tanwar, P., Yang, H.-Y., Tafti, F., Cuono, G., Islam, R., Singh, B., Lynnyk, A., et al.: Sign change of anomalous Hall effect and anomalous Nernst effect in the Weyl semimetal CeAlSi . *Physical Review B* **107**(8), 085102 (2023) <https://doi.org/10.1103/physrevb.107.085102>

- [41] Kolincio, K.K., Hirschberger, M., Masell, J., Arima, T.-h., Nagaosa, N., Tokura, Y.: Kagome lattice promotes chiral spin fluctuations. *Physical Review Letters* **130**(13), 136701 (2023) <https://doi.org/10.1103/physrevlett.130.136701>
- [42] Kanazawa, N., Kubota, M., Tsukazaki, A., Kozuka, Y., Takahashi, K.S., Kawasaki, M., Ichikawa, M., Kagawa, F., Tokura, Y.: Discretized topological Hall effect emerging from skyrmions in constricted geometry. *Phys. Rev. B* **91**, 041122 (2015) <https://doi.org/10.1103/PhysRevB.91.041122>
- [43] Gallagher, J.C., Meng, K.Y., Brangham, J.T., Wang, H.L., Esser, B.D., McComb, D.W., Yang, F.Y.: Robust Zero-Field Skyrmion Formation in FeGe Epitaxial Thin Films. *Phys. Rev. Lett.* **118**, 027201 (2017) <https://doi.org/10.1103/PhysRevLett.118.027201>
- [44] Li, Y., Kanazawa, N., Yu, X.Z., Tsukazaki, A., Kawasaki, M., Ichikawa, M., Jin, X.F., Kagawa, F., Tokura, Y.: Robust Formation of Skyrmions and Topological Hall Effect Anomaly in Epitaxial Thin Films of MnSi. *Phys. Rev. Lett.* **110**, 117202 (2013) <https://doi.org/10.1103/PhysRevLett.110.117202>
- [45] Kresse, G., Hafner, J.: Ab initio molecular dynamics for liquid metals. *Physical review B* **47**(1), 558 (1993) <https://doi.org/10.1103/PhysRevB.47.558>
- [46] Kresse, G., Furthmüller, J.: Efficiency of ab-initio total energy calculations for metals and semiconductors using a plane-wave basis set. *Computational materials science* **6**(1), 15–50 (1996) [https://doi.org/10.1016/0927-0256\(96\)00008-0](https://doi.org/10.1016/0927-0256(96)00008-0)
- [47] Kresse, G., Joubert, D.: From ultrasoft pseudopotentials to the projector augmented-wave method. *Physical review b* **59**(3), 1758 (1999) <https://doi.org/10.1103/PhysRevB.59.1758>
- [48] Perdew, J.P., Burke, K., Ernzerhof, M.: Generalized gradient approximation made simple. *Physical review letters* **77**(18), 3865 (1996) <https://doi.org/10.1103/PhysRevLett.77.3865>
- [49] Cheong, S.-W., Huang, F.-T.: Altermagnetism with non-collinear spins. *npj Quantum Materials* **9**(1), 13 (2024) <https://doi.org/10.1038/s41535-024-00626-6>
- [50] Mostovoy, M.: Phenomenology of altermagnets. *Applied Physics Letters* **127**(6) (2025) <https://doi.org/10.1063/5.0283630>